

Perfect Linear Optics using Silicon Photonics

Miltiadis Moralis-Pegios^{1*†}, George Giamougiannis^{1†}, Apostolos Tsakyridis¹, David Lazovsky²,
Nikos Pleros¹

¹*Department of Informatics, Aristotle University of Thessaloniki, 54124, Thessaloniki, Greece*

²*Celestial AI, 2962 Bunker Hill Ln, Suite 200, Santa Clara, CA 95054, USA*

[†]The authors contributed equally to this work.

[*mmoralis@csd.auth.gr](mailto:mmoralis@csd.auth.gr)

Abstract

In recent years, there has been growing interest in using photonic technology to perform the underlying linear algebra operations required by different applications, including neuromorphic photonics, quantum computing and microwave processing, mainly aiming at taking advantage of the silicon photonics' (SiPho) credentials to support high-speed and energy-efficient operations. Mapping, however, a targeted matrix with absolute accuracy into the optical domain remains a huge challenge in linear optics, since state-of-the-art linear optical circuit architectures are highly sensitive to fabrication imperfections. This leads to reduced fidelity metrics that degrade faster as the insertion losses of the constituent optical matrix node or the matrix dimensions increase. In this work, we present for the first time a novel coherent SiPho crossbar (Xbar) that can support on-chip fidelity restoration while implementing linear algebra operations, realizing the first experimental demonstration of perfect on-chip arbitrary linear optical transformations. We demonstrate the experimental implementation of 10000 arbitrary linear transformations in the photonic domain achieving a record-high fidelity of $99.997\% \pm 0.002$, limited mainly by the statistical error enforced by the measurement equipment. Our work represents the first integrated universal linear optical circuit that provides almost unity and loss-independent fidelity in the realization of arbitrary matrices, opening new avenues for exploring the use of light in resolving universal computational tasks.

1. Introduction

Linear optical circuitry has been recently brought into the spotlight as a powerful tool for a wide range of applications, including microwave and quantum optical signal processing¹⁻², as well as next-generation bio-inspired computing architectures. Recent architectural breakthroughs³⁻⁹ together with the growing maturity of SiPho platforms¹⁰, which allows the deployment of hundreds to thousands of miniaturized photonic components into a single chip, has elevated integrated photonics to the platform of choice for next generation linear optical circuitry, with recent experimental demonstrations confirming the potential of silicon photonics to break through the stability, scale and energy consumption barriers of alternative platforms, such as bulk optics¹¹.

The dominant approach in integrated linear photonic circuitry architectures is based until now on manipulating light via coherent interferometric meshes¹²⁻¹⁴ that target the implementation of unitary linear transformations. These layouts rely on U(2)-based matrix decomposition schemes and cascaded stages of 2×2 Mach-Zehnder interferometer (MZI) blocks. Despite their simplicity, symmetrical layout and impressive academic and industrial demonstrations¹⁵⁻¹⁶, these approaches are burdened by inherent architectural deficiencies that mainly originate from the accumulating nature of fabrication imperfections across their cascaded nodes. This has a significant impact to their size scaling and overall performance credentials¹⁴ i.e., fidelity, programming complexity, processing bandwidth, energy- and footprint-efficiency. More specifically, the hardware implementation of such meshes suffers from (i) insertion loss (IL) that scales nonlinearly to the loss of the constituent matrix node, limiting in this way the deployment of large-size photonic processors, (ii) high-complexity programming¹⁷, which becomes more pronounced when high-scale implementations are targeted, (iii) limited computing nodes' update speed, since cascading several high-speed and, as such, relatively high IL nodes, converges rapidly to prohibitive power budgets¹⁴, (iv) reduced and non-restorable fidelity due to the intrinsic differential optical path losses, negating any perspective for perfectly mapping a targeted linear transformation into the optical domain, and finally (v) an application portfolio that is inherently confined to unitary transformations¹²⁻¹³, with their

universalization requiring the adoption of Singular Value Decomposition (SVD) schemes¹⁹ with two unitary MZI meshes around a diagonal optical matrix, which pronounces all the above disadvantages²⁰. Nevertheless, the advent of photonic integration technology has managed to yield ultra-low loss 2×2 MZI technology that allowed for significant progress in the scalability and IL performance of unitary and universal linear optical circuitry, although not being able yet to combine high-bandwidth operation with this ultra-low loss envelope. Programming complexity and mesh calibration has been also facilitated through self-configured linear optics¹⁹. However, fidelity restoration and inaccurate mapping of the linear transformations comprise native architectural drawbacks in these layouts; despite the fidelity improvements obtained through MZI node loss reductions, the inherent presence of differential paths cancels any perspective for restoring the circuit fidelity and accurately representing a targeted matrix into the optical experimental domain.

In this paper, we present for the first time, to the best of our knowledge, perfect on-chip universal linear optics via a SiPho linear operator that is capable of breaking through the IL-fidelity-scale trade-offs of MZI-mesh based approaches, demonstrating experimentally perfect linear optical transformations even when high-loss optical matrix nodes are employed. This performance is enabled by fabricating a novel coherent photonic Crossbar (Xbar) architecture^{14,21,22} onto the silicon platform, investing in a linear optical circuit architecture that demarcates from traditional unitary-based approaches and promotes a distributed tree-based power split-and-recombination stage together with a bijective weight mapping. The fabricated 4×4 SiPho Xbar employs 50GHz SiGe EAMs for the encoding of both the 4-element input vector and the 4×4 transformation matrix, using in addition silicon-based thermo-optic (TO) phase shifters (PSs) for fine phase control. We report an experimental record-high on-chip fidelity of 99.997±0.002% in the implementation of 10000 arbitrary linear transformations, a performance converging to the measurement uncertainty originating from the employed experimental equipment, highlighting both the fidelity restoration capabilities of our architecture and the scalable and low-complexity programming required.

2. Crossbar architecture, photonic chip programming

A. Photonic Xbar architecture

The architecture of the proposed SiPho Xbar¹⁴ is illustrated in Fig. 1 (a). As extensively analyzed in our previous work¹⁴, an $N \times M$ Xbar operates as a vector-matrix linear operator via the direct mapping of the scalars of an N -elements-long vector X and an $N \times M$ matrix W into individual photonic modulating components. The Xbar architecture exploits the coherent recombination of modulated light via MZIs that are nested into splitting and recombining tree configurations. In particular, the N -elements of the input vector X are encoded to equivalent modulators located at the $\#N$ outputs of a $1:N$ splitter, with the resulting modulated light getting equally shared among the $\#M$ Xbar columns. A modulator at each row of each column weighs the respective element of X , according to the corresponding element of W . The weighted vector's elements of the $\#N$ rows of each column are summed via an $N:1$ combiner, completing the required linear transformation in the electric field. The vector and matrix element encoding sections are highlighted in the red and yellow rectangles of Fig. 1 (a), respectively.

Figure 1 (b) depicts a microscope photo of the wirebonded 4×4 SiPho Xbar prototype, that was fabricated on imec's ISIPP50G platform using pdk-ready components. SiGe EAMs of 50 μm length and a 3dB bandwidth of 50 GHz²³ were deployed for the vector and matrix element encoding, with the matrix element encoding cells being additionally equipped with TO PSs in order to encode the $|X_i * w_{i,j}|$ product sign and ensure proper biasing of the nested MZIs²⁴. Details of the experimental setup utilized for the chip characterization are provided in Supplementary section 1.

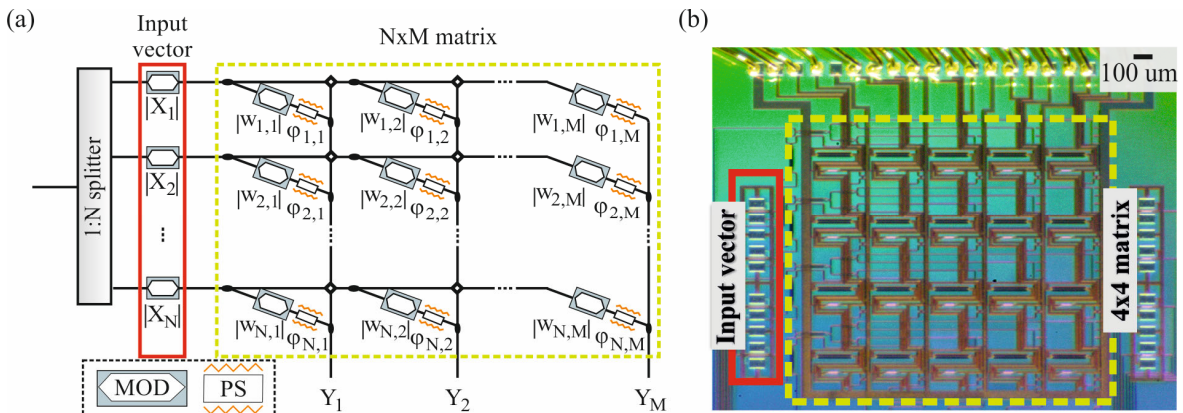


Fig. 1: (a) $N \times M$ Crossbar architecture. (b) 4×4 SiPho Xbar chip.

B. Silicon photonic Xbar Calibration

The effectiveness of a linear operator predominantly hinges on the programming precision of its nodes, that consequently translates into the accurate execution of the targeted linear matrix transformations. In our architecture, where EAMs comprise the basic constituent computational building blocks, our first step builds upon the assumption that all EAMs comprise identical devices. As such, we designed, fabricated and characterized a standalone EAM that shared the same design properties with the ones employed in the fabricated 4×4 Xbar of Fig. 1(b). The experimentally measured performance metrics of the stand-alone EAM were used as a reference point for the induced IL and reverse bias versus attenuation relationship of the Xbar's constituent EAM devices (see Supplementary section 1). While this approach offers a baseline estimation of the Xbar's operational parameters, the unavoidable fabrication-induced performance variation between each constituent EAM, as well as the fabrication imperfections of the employed waveguide crossings and the horizontal and vertical light splitting stages, lead to imprecise mapping of the transformation matrix elements to the silicon photonic Xbar and, as a consequence, to imperfect fidelity transformations.

The bijective weight-to-node mapping supported by the Xbar architecture allows to compensate for the fabrication imperfections and to ensure a high-accuracy calibration procedure, taking advantage of the absence of any interdependence between the matrix nodes of different columns. A low complexity $O(N)$ hardware-aware (HA) programming algorithm was developed, with Figure 2 (a) illustrating the developed experimental testbed for the HA programming model when applied to the 1st column of our fabricated SiPho Xbar. With the input vector encoding EAMs being in their transparent state ($V=0$), the DC control plane was programmed to bias the node-EAMs of the 4 rows at discrete bias levels, within the range $B = \{0, -1, -2, -3\}V$ (see Supplementary section 2). Followingly, the output Y was consecutively recorded via a power meter for all 256 ($=4^4$) possible linear transformations combination sets. When the nested MZIs of the 1st column get tuned to their fully-constructive interference state, then the column output equals $Y_1 = \sum_{r=1}^4 (IL_r + EAM_{ER_r}(V))$, $V \in B$, with IL_r corresponding to the excess loss introduced by all column's

components at row $\#r$ i.e., splitters, combiners, waveguide crossings, EAMs, and PSs, while $EAM_ER_r(V)$ corresponds to the absorption-induced attenuation of the node-EAMs of row $\#r$ when biased with a voltage $V \in B$. Given the unavoidable fabrication variation-induced discrepancy between the constituent IL_r and $EAM_ER_r(V)$ values and the baseline performance of the standalone EAM, we developed a linear regression algorithm (see Methods and Supplementary for more details) that exploits the experimentally obtained linear transformations to approximate the undetermined parameters.

In order to ease the understanding of the programming procedure, we indicatively illustrate in Fig. 2 (b) the sum of IL_r and $EAM_ER_r(V)$ experimental values for the 4 constituent paths of the 1st Xbar column with $r = [1,2,3,4]$. These values were calculated via the HA model when a single node is driven in the range $B = \{0, -1, -2, -3\}V$ and the remaining 3 EAMs are driven at 0V bias, revealing the divergence from the expected performance when using the standalone EAM metrics (baseline model). Figure 2 (c) schematically captures the effectiveness of the developed HA

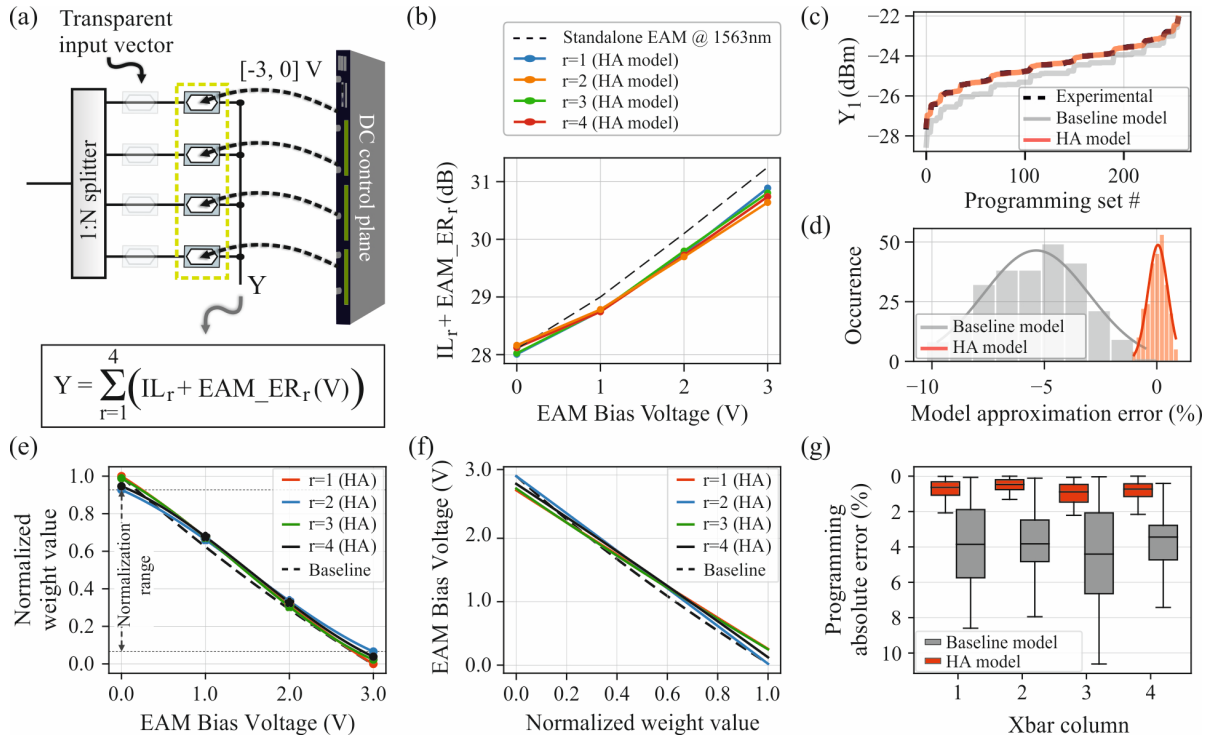


Fig. 2: (a) Testbed for the programming of Xbar’s 1st column. (b) Relation of Xbar rows’ attenuation factor (photonic axes IL + EAMs extinction ratio) with their biasing voltage. (c) Experimental power levels obtained at Xbar’s 1st column output for 256 different EAM biasing voltage sets and respective theoretically expected output power levels when using the baseline and HA programming models. (d) Baseline and HA model approximation error histograms (e) Experimentally derived relation of row’s weighting values versus EAMs bias voltage for the 1st column of the Xbar. (f) EAM bias voltage vs weight value “look-up” table. (g) Experimentally obtained absolute error when programming the Xbar by the baseline and HA model for all the columns.

programming model, by putting in juxtaposition the experimentally measured Y_1 output for the #256 linear transformation sets (black dashed line) with respect to the theoretically calculated Y_1 output when using the baseline programming model (grey curve) and the theoretically calculated Y_1 output when using the HA programming model (orange curve), revealing the excellent matching between the experimental curve and the curve calculated via the HA model. A quantitative representation of the model's accuracy in describing the underlying hardware parameters is presented in Fig. 2 (d), where the error of the baseline and HA programming model outputs with respect to the experimentally obtained response is plotted with the grey and orange histograms, respectively. Fitting a Gaussian distribution into the acquired error values results in mean and standard deviation values that equal -5.45 and 2.04, and $\sim 2 \cdot 10^{-3}$ and 0.41 for the baseline and HA models respectively, revealing the lack of a biased-error parameter in our HA-model and a significantly lower standard deviation. The same procedure was followed for the remaining 3 Xbar columns and 12 constituent EAM-based nodes, revealing a small deviation of <2% in the derived mean and standard deviation values.

Having estimated the individual parameters of the constituent EAM-based nodes with high-precision, we proceed by developing an algorithm that is capable of compensating for their performance divergence and providing the transformation matrix encoding map for arbitrary values. The first step includes the correlation of the required EAM bias voltage to each row's weighing factor by normalizing the $[IL_r + EAM_ER_r(V)]$ values to $[0, 1]$, as shown in Fig. 2 (e), where the same coloring with Fig. 2 (b) was employed to discriminate between each row's respective curve. A 2nd order polynomial fit was applied to express the transfer function of each EAM, with high precision across the whole B range $[0,3]$. Thereafter, towards alleviating the inter-row weighting divergence, all 4 curves were bounded to the lowest and highest weight value of the 4 Xbar rows, highlighted in Fig. 2(e), when the respective node-EAMs are biased at 0 and -3 Vs, respectively, and normalized again to the $[0, 1]$ range. Finally, the targeted look-up table can be formulated by inverting the fitted transfer functions, as depicted in Fig. 2 (f). A set of #100 arbitrary transformation vectors were then generated and encoded at each Xbar column individually towards evaluating the accuracy of the

developed HA programming model and the weighting calibration process. Figure 2 (g) indicates the achieved absolute error values, normalized in percentage values through $E = \frac{P_{expected} - P_{experimental}}{P_{expected}} * 100$, with $P_{expected}$ corresponding to the expected output optical power for the given transformation and $P_{experimental}$ to the measured optical power at the Xbar output, for a set of 100 arbitrary matrix transformations for all 4 Xbar columns, with the red and grey bars corresponding to the HA and baseline programming model, respectively. As can be observed, the HA model achieved an *absolute* average error reduction of 3.2% compared to the baseline programming. Fitting a Gaussian distribution to the calculated error values, using their raw i.e., not-absolute values, concludes to mean and standard deviation values, expressed in normalized percentage values, of $\mu = [-0.39, -0.17, 0.04, 0.19]\%$ and $\sigma = [0.69, 0.6, 1.06, 0.92]\%$ for all 4 Xbar columns, respectively. In order to benchmark the achieved programming error versus the measurement uncertainty originating from the experimental setup, we performed a 1-hour long stability measurement using the experimental chain of Laser-Input GC-Chip Transmission-GC-PM, while applying 0 V to the constituent EAM and TO-PS. The measurements across the 4 column outputs revealed standard deviations in the range of [0.014, 0.028] dB that correspond to $\sigma_{equip} = [0.3-0.6]\%$, highlighting in this way that the majority of the programming error originates from the environmental and mechanical perturbations during the PIC measurement procedure.

3. Crossbar fidelity restoration & experimental results

A. Inter-column fidelity restoration

Following the intra-column calibration procedure, we proceed by quantifying the fabrication error-induced inter-column differential loss and showcasing the functionality of the fidelity restoration mechanism of the Xbar photonic linear processor. Figure 3 (a) illustrates the distribution of the optical powers emerging at all 4 Xbar column outputs, when 100 arbitrary matrices are experimentally enforced on an all-one input vector. Fitting each column's output power histogram to a gaussian distribution and comparing the resulting mean values allows for the quantification of the inter-column differential loss. As can be observed, the 4 Xbar columns exhibited an average optical loss of 24.2 dB,

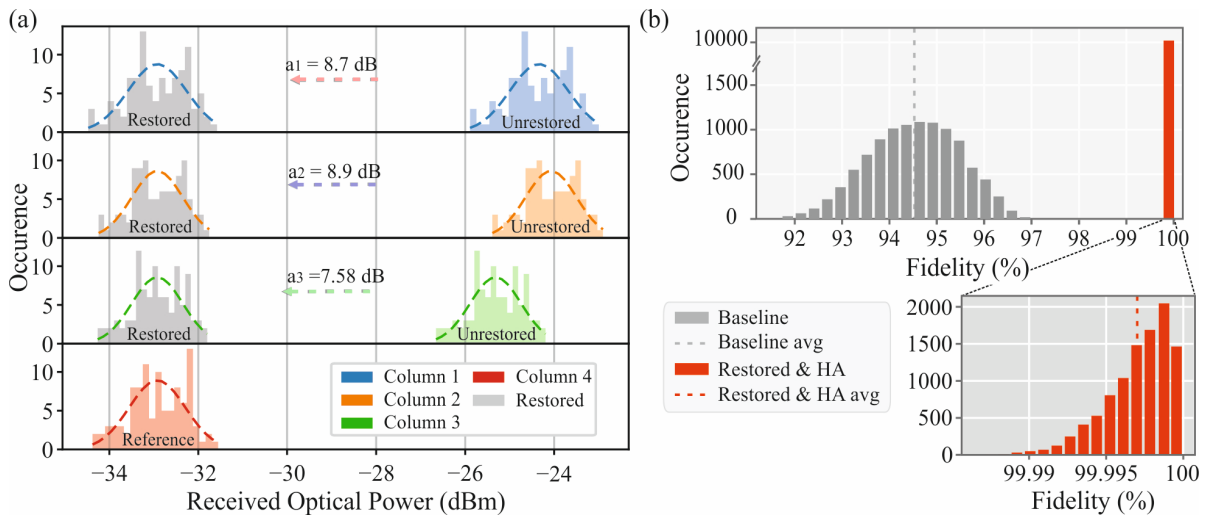


Fig. 3: (a) Xbar fidelity restoration mechanism illustration for 0 dBm input power. (b) Experimentally obtained fidelity in the execution of #10000 arbitrary linear transformation matrices when the Xbar is programmed with the baseline model (grey) and the HA model and restoration procedure (red).

24.01 dB, 25.32 dB and 32.9 dB, respectively, with the maximum differential loss of 8.9 dB observed between columns #2 and #4 and owing mainly to the damaged I/O coupling in the 4th column. The average differential loss when only columns #1-#3 are considered ranged between [0.25 dB-1.32 dB], which is in line with the performance variation expected by fabrication variations at each constituent photonic building blocks, i.e., directional couplers, waveguide crossings, EAMs and MMIs. Despite the excess losses of column #4, the absence of interdependency between the elements of the Xbar output vector allows for the realization of an inter-column loss-balanced layout¹⁴. This can be readily achieved through selecting the gaussian fitted-mean value of the column with the lowest output power (column #4) and enforcing an attenuation factor a_i at the output of every other i^{th} column, with a_i equaling to the differential loss between column #4 and column # i . The addition of the external attenuation factors at the outputs of the three Xbar columns #1-#3 leads to a loss-balanced Xbar output vector and forms the fidelity restoration stage, as has been theoretically analyzed in¹⁴. A schematic representation of this procedure, when selecting column 4 as the reference column, is shown in Fig. 3 (a). The arrows correspond to the enforced attenuation factors a_i and the grey-colored histograms to the column output power distributions after the fidelity restoration process has been applied.

B. Experimental linear transformations fidelity of arbitrary matrices

The performance of the photonic Xbar as a linear operator was finally assessed by experimentally implementing a set of 10000 [4×4] arbitrary transformation matrices, when considering an all-one input vector, and measuring the achieved fidelity. Fidelity has been defined as the Frobenious inner product of the targeted (Y_{targ}) and the experimentally obtained (Y_{exp}) output vectors, with the respective mathematical formula being: $F(Y_{exp}, Y_{targ}) =$

$$\left| \frac{tr(Y_{targ}^T * Y_{exp})}{\sqrt{tr(Y_{targ}^T * Y_{targ}) * tr(Y_{exp}^T * Y_{exp})}} \right|.$$

Figure 3(b) reveals the distribution of the achieved fidelities when the Xbar is programmed utilizing (i) a “baseline” matrix programming, that neither takes into account the fabrication variations of the constituent EAM-based nodes nor utilizes the fidelity restoration stage for differential loss balancing, and (ii) a fidelity restored and HA matrix programming that compensates for the fabrication imperfections. As can be observed our approach significantly increases the achieved fidelity from $94.35 \pm 0.693\%$ to an almost unity fidelity of $99.997 \pm 0.002\%$, with the $\pm 0.002\%$ converging to the statistical error induced by the measurement procedure, highlighting in this way the substantial fidelity restoration credentials of our photonic Xbar architecture.

4. Discussion

High-fidelity performance is a prerequisite for the majority of the targeted use-cases, becoming even more pronounced in specialized tasks, e.g., in quantum gates where $>99\%$ fidelity values are required²⁵, in safety critical NN workloads for automotive or Unmanned Aerial Vehicle applications²⁶, and

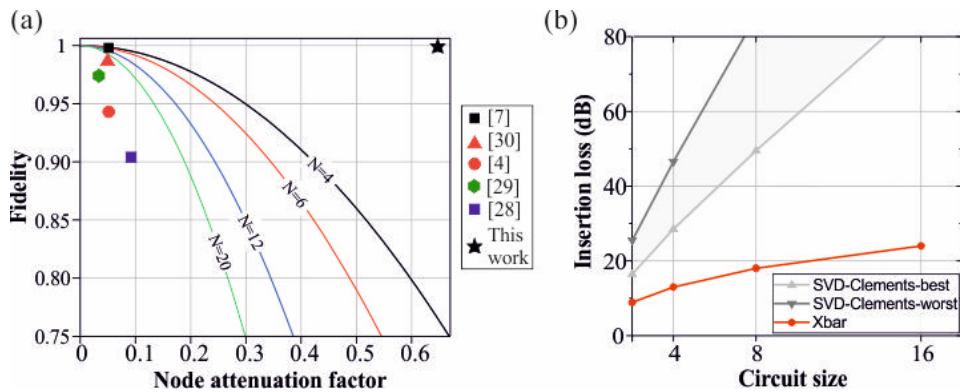


Fig. 4: (a) Theoretically and experimentally obtained fidelity values of unitary-based architectures juxtaposed to the experimentally obtained fidelity of this work. (b) Theoretically expected IL values calculated of $N \times N$ Xbar (red) and SVD-Clements (grey) architectures for a node loss of 4.5 dB.

in high-precision Optical Beamformer networks for LiDAR and microwave photonics²⁷. In order to benchmark the experimentally demonstrated fidelity performance of our SiPho chip versus state-of-the-art approaches, Fig. 4 (a) puts in juxtaposition: (i) The theoretical fidelity upper bound (see Methods) versus node attenuation factor and for different radii between $N=4$ and $N=20$ ^{4,7,28-30}, for photonic processors that follow the prominent unitary-based architecture. Node attenuation factor is defined as $n_{Att} = 1 - 10^{ILnode/10}$, with $ILnode$ denoting the IL per node. (ii) The experimentally reported fidelity of recent photonic linear processor prototypes, including our 4×4 Xbar demonstrator, with the scatter plot color corresponding to the prototype's scale and the respective theoretical curve. This analysis leads to three important conclusions (a) The achieved fidelity of an SVD-Clements optical processor heavily depends on both the scale and the IL of the constituent weighting nodes, effectively reaching a hard-limit based on the current SiPho platforms technology level. (b) The high-programming complexity of interdependent MZI-mesh architecture inevitably leads to high complexity calibration algorithms and subsequently to a discrepancy between the maximum theoretical limit and the achieved experimental fidelity, (c) The unique fidelity credentials of the proposed Xbar architecture are validated through our experimental demonstration, highlighting that our approach leads to easily calibrated and fidelity restorable layouts that are capable of breaking the scale plus IL/node tradeoff and reaching record high fidelities. This unique property can also unlock the employment of the Xbar architecture in applications where the operational speed is critical, i.e., Data Centre cybersecurity³¹, training of Deep Learning models³²⁻³³, inference with tiled matrix multiplication etc²¹, since it can tolerate the high-loss that is typically associated with high-speed optical modulators, without sacrificing fidelity performance. This architectural advantage extends also to the total circuit IL, as highlighted in Fig. 4 (b) that illustrates the total IL values of both the Xbar and the SVD-Clements layouts for circuits sizes up to 64 and for a relatively high node IL value of $ILnode = 4.5 \text{ dB}$, as has been the case in the fabricated 4×4 EAM-based Xbar SiPho chip. As can be observed, the linear scaling of the Xbar IL against the node IL¹⁴ allows for practical implementations of up to 64×64 radii, considering a total IL limit of less than 40dB. On the contrary,

the use of node cascades in the case of the SVD-Clements layout leads rapidly to prohibitively high IL values for matrix sizes larger than 4×4 .

5. Conclusions

In summary, we presented the first SiPho Xbar architecture that can execute perfect universal linear optical operations, while also enabling ultra-high speed computations. By developing a generic, hardware-aware programming procedure, we experimentally performed 10000 arbitrary linear transformations on a 4×4 SiPho chip with a record-high fidelity of $99.997\% \pm 0.002$ that converges to the statistical error induced by our measurement equipment. This performance allows for accurate experimental realizations of linear transformations, overcoming the inherent fidelity limits of 2×2 MZI-based interferometric unitary and universal layouts. Its experimental IL-fidelity performance reveals its unique credentials to sustain perfect linear operations even when high-loss optical nodes are employed, paving new inroads that expand along high-speed reconfigurable optical matrix realizations, while still retaining wavelength as an extra degree of freedom³⁴⁻³⁵. This can lead to new application segments, by operating either as an application-specific processor, following the graphics processing units (GPUs) paradigm, or as a universal linear processor by selecting the technological building blocks and its operational clock frequencies accordingly.

References

1. Bogaerts, W., Pérez, D., Capmany, J. et al. Programmable photonic circuits. *Nature* 586, 207–216 (2020). <https://doi.org/10.1038/s41586-020-2764-0>
2. Flamini, F., Spagnolo, N., Viggianiello, N. et al. Benchmarking integrated linear-optical architectures for quantum information processing. *Sci Rep* 7, 15133 (2017). <https://doi.org/10.1038/s41598-017-15174-2>
3. Antonio Ribeiro, Alfonso Ruocco, Laurent Vanacker, and Wim Bogaerts, "Demonstration of a 4×4 -port universal linear circuit," *Optica* 3, 1348-1357 (2016)
4. J. Carolan, C. Harrold, C. Sparrow, E. Martín-López, N. J. Russell, J. W. Silverstone, P. J. Shadbolt, N. Matsuda, M. Oguma, M. Itoh, G. D. Marshall, M. G. Thompson, J. C. F.

- Matthews, T. Hashimoto, J. L. O'Brien, and A. Laing, "Universal linear optics," *Science* 349, 711–716 (2015).
5. Capmany, J., Gasulla, I. & Pérez, D. The programmable processor. *Nature Photon* 10, 6–8 (2016).
 6. M. Miscuglio, V.J. Sorger, "Photonic Tensor cores for machine learning", *Appl. Phys. Rev.*, vol.7 issue 3 (2020).
 7. Y. Shen, N. C. Harris, S. Skirlo, M. Prabhu, T. Baehr-Jones, M. Hochberg, X. Sun, S. Zhao, H. Larochelle, D. Englund, and M. Soljačić, "Deep learning with coherent nanophotonic circuits," *Nat. Photonics* 11, 441–446 (2017).
 8. Zhang, H., Gu, M., Jiang, X.D. et al. An optical neural chip for implementing complex-valued neural network. *Nat Commun* 12, 457 (2021). <https://doi.org/10.1038/s41467-020-20719-7>
 9. Feldmann, J., Youngblood, N., Karpov, M. et al. Parallel convolutional processing using an integrated photonic tensor core. *Nature* 589, 52–58 (2021). <https://doi.org/10.1038/s41586-020-03070-1>
 10. X. Chen et al., "The Emergence of Silicon Photonics as a Flexible Technology Platform," in *Proceedings of the IEEE*, vol. 106, no. 12, pp. 2101-2116, Dec. 2018, doi: 10.1109/JPROC.2018.2854372
 11. George Dabos, Dimitris V. Bellas, Ripalta Stabile, Miltiadis Moralis-Pegios, George Giamougiannis, Apostolos Tsakyridis, Angelina Totovic, Elefterios Lidorikis, and Nikos Pleros, "Neuromorphic photonic technologies and architectures: scaling opportunities and performance frontiers [Invited]," *Opt. Mater. Express* 12, 2343-2367 (2022).
 12. M. Reck, A. Zeilinger, H. J. Bernstein and P. Bertani, "Experimental realization of any discrete unitary operator," *Phys. Rev. Lett.* 73, 58–61 (1994).
 13. W. R. Clements, P. C. Humphreys, B. J. Metcalf, W. Steven Kolthammer and I. A. Walmsley, "Optimal design for universal multiport interferometers," *Optica* 3, 1460–1465 (2016).
 14. G. Giamougiannis, A. Tsakyridis, Y. Ma, A. Totović, M. Moralis-Pegios, D. Lazovsky, et al.,

- A coherent photonic crossbar for scalable universal linear optics, *Journal of Lightwave Technology*. 41 (2023) 2425–2442. doi:10.1109/jlt.2023.3234689.
15. Hot Chips 2020 Live Blog: Silicon Photonics for AI | Accessed: Mar. 23, 2023. [Online]. Available: <https://www.anandtech.com/show/16010/hot-chips-2020-live-blog-silicon-photonics-for-ai-600pm-pt>.
 16. Lightelligence PACE. Available online: <https://www.lightelligence.ai/index.php/product/index/2.html>. Accessed April 2023]
 17. Hamerly, R., Bandyopadhyay, S. & Englund, D. Asymptotically fault-tolerant programmable photonics. *Nat Commun* 13, 6831 (2022). <https://doi.org/10.1038/s41467-022-34308-3>
 18. G. Giamougiannis, A. Tsakyridis, M. Moralis-Pegios, A.R. Totovic, M. Kirtas, N. Passalis, et al., Universal Linear Optics Revisited: New perspectives for neuromorphic computing with Silicon Photonics, *IEEE Journal of Selected Topics in Quantum Electronics*. 29 (2023) 1–16. doi:10.1109/jstqe.2022.3228318.
 19. D. A. B. Miller, "Self-configuring universal linear optical component [Invited]", *Photon. Res.*, vol. 1, pp. 1-15, 2013
 20. D. A. B. Miller, "How complicated must an optical component be?", *J. Opt. Soc. Am. A* 30, 238-251 (2013)
 21. G. Giamougiannis, A. Tsakyridis, M. Moralis-Pegios, G. Mourgias-Alexandris, A.R. Totovic, G. Dabos, et al., Neuromorphic silicon photonics with 50GHz tiled matrix multiplication for deep-learning applications, *Advanced Photonics*. 5 (2023). doi:10.1117/1.ap.5.1.016004.
 22. A. Tsakyridis, G. Giamougiannis, M. Moralis-Pegios, G. Mourgias-Alexandris, A.R. Totovic, M. Kirtas, et al., Universal linear optics for ultra-fast neuromorphic silicon photonics towards FJ/Mac and TMAC/sec/mm² engines, *IEEE Journal of Selected Topics in Quantum Electronics*. (2022) 1–15. doi:10.1109/jstqe.2022.3219288.
 23. M. Pantouvaki, S.A. Srinivasan, Y. Ban, P. De Heyn, P. Verheyen, G. Lepage, et al., Active components for 50 GB/s NRZ-ook optical interconnects in a silicon photonics platform,

- Journal of Lightwave Technology. 35 (2017) 631–638. doi:10.1109/jlt.2016.2604839.
24. G. Mourgias-Alexandris, A. Totovic, A. Tsakyridis, N. Passalis, K. Vyrsoinos, A. Tefas, et al., Neuromorphic photonics with coherent linear neurons using dual-IQ modulation cells, *Journal of Lightwave Technology*. 38 (2020) 811–819. doi:10.1109/jlt.2019.2949133.
 25. S. Shi, B. Xu, K. Zhang, G.-S. Ye, D.-S. Xiang, Y. Liu, et al., High-fidelity photonic quantum logic gate based on near-optimal Rydberg single-photon source, *Nature Communications*. 13 (2022). doi:10.1038/s41467-022-32083-9.
 26. S. Alaba, , A comprehensive survey of Deep Learning multisensor fusion-based 3D object detection for autonomous driving: Methods, challenges, open issues, and Future Directions [Preprint]. doi:10.36227/techrxiv.20443107.v1.(2022)
 27. X. Zhang, K. Kwon, J. Henriksson, J. Luo, M.C. Wu, A large-scale microelectromechanical-systems-based Silicon Photonics Lidar, *Nature*. 603 (2022) 253–258. doi:10.1038/s41586-022-04415-8.
 28. C. Taballione, R. van der Meer, H.J. Snijders, P. Hooijschuur, J.P. Epping, M. de Goede, et al., A universal fully reconfigurable 12-mode quantum photonic processor, *Materials for Quantum Technology*. 1 (2021) 035002. doi:10.1088/2633-4356/ac168c.
 29. D. Smith, C. Taballione, M.C. Anguita, M. De Goede, P. Venderbosch, B. Kassenberg, et al., A universal 20-mode quantum photonic processor in silicon nitride, *Optica Advanced Photonics Congress 2022*. (2022). doi:10.1364/iprsn.2022.itu4b.2.
 30. S. Bandyopadhyay, A. Sludds, S. Krastanov, R. Hamerly, N. Harris, D. Bunandar, M. Streshinsky, M. Hochberg, D. Englund, “Single chip photonic deep neural network with accelerated training”, arXiv:2208.01623 [cs.ET], Aug. (2022)
 31. A. Tsakyridis, G. Giamougiannis, M. Moralis-Pegios, G. Mourgias-Alexandris, A.R. Totovic, G. Dabos, et al., DDOS attack identification via a silicon photonic deep neural network with 50 GHz input and Weight Update, *Optical Fiber Communication Conference (OFC) 2023*. (2023). doi:10.1364/ofc.2023.w3g.1.

32. M. Moralis-Pegios, G. Mourgias-Alexandris, A. Tsakyridis, G. Giamougiannis, A. Totovic, G. Dabos, et al., Neuromorphic silicon photonics and hardware-aware deep learning for high-speed inference, *Journal of Lightwave Technology*. 40 (2022) 3243–3254. doi:10.1109/jlt.2022.3171831.
33. Giamougiannis, George, Tsakyridis, Apostolos, Moralis-Pegios, Miltiadis, Pappas, Christos, Kirtas, Manos, Passalis, Nikolaos, Lazovsky, David, Tefas, Anastasios and Pleros, Nikos. "Analog nanophotonic computing going practical: silicon photonic deep learning engines for tiled optical matrix multiplication with dynamic precision" *Nanophotonics*, vol. 12, no. 5, 2023, pp. 963-973. <https://doi.org/10.1515/nanoph-2022-0423>
34. A. Totovic, C. Pappas, M. Kirtas, A. Tsakyridis, G. Giamougiannis, N. Passalis, et al., WDM equipped universal linear optics for programmable neuromorphic photonic processors, *Neuromorphic Computing and Engineering*. 2 (2022) 024010. doi:10.1088/2634-4386/ac724d.
35. Totovic, A., Giamougiannis, G., Tsakyridis, A. et al. Programmable photonic neural networks combining WDM with coherent linear optics. *Sci Rep* 12, 5605 (2022). <https://doi.org/10.1038/s41598-022-09370-y>
36. ID Photonics. (n.d.). Cobrite DX tunable laser [Product description]. Retrieved from <https://id-photonics.com/products-solutions/tunable-lasers/cobrite-portfolio/cobrite-dx>
37. Keysight Technologies. (2023). N7745A Optical Multiport Power Meter [Product description]. Retrieved from <https://www.keysight.com/us/en/product/N7745A/optical-multiport-power-meter-8-sensor-ports.html>
38. Jahvani, M. and Guay, M. (2022) "A distributed least-squares solver for linear systems of algebraic equations," *IFAC-PapersOnLine*, 55(7), pp. 804–808. Available at: <https://doi.org/10.1016/j.ifacol.2022.07.543>.]
39. S. Garg, J. Lou, A. Jain, Z. Guo, B. J. Shastri and M. Nahmias, "Dynamic Precision Analog Computing for Neural Networks," in *IEEE Journal of Selected Topics in Quantum*

Electronics, vol. 29, no. 2: Optical Computing, pp. 1-12, March-April 2023, Art no. 6100412,
doi: 10.1109/JSTQE.2022.3218019

Acknowledgements

The authors would like to thank Dr. Nikos Bamiedakis for fruitful discussions. The work was in part funded by the EU-project PlasmoniAC (871391) and EU-project SiPHO-G (779664)

Author Contributions

Miltiadis Moralis-Pegios, George Giamougiannis, Apostolos Tsakyridis and Nikos Pleros conceived the experiment. Miltiadis Moralis-Pegios and George Giamougiannis deployed the experimental setup, performed the experiment and processed the experimental results. George Giamougiannis, Apostolos Tsakyridis and Nikos Pleros performed the simulation analyses. David Lazovsky and Nikos Pleros conceived the circuit architecture and secured funding for chip fabrication and packaging, while David Lazovsky, Nikos Pleros and Miltiadis Moralis-Pegios contributed to the mask design. All authors discussed the results and wrote the manuscript.

Data availability

The data that support the plots within this paper and other findings of this study are available from the corresponding authors upon reasonable request.

Methods

Experimental setup and SiPho processor characteristics

The 4×4 Xbar was fabricated in IMEC’s ISSIPP50G SiPho platform using established building blocks from the supplied process design kit (PDK). A laser source was utilized to generate a continuous wave beam that was injected into the Xbar chip input port through a fiber array, while a polarization controller was employed to align the input polarization to the TE-optimized grating couplers, exhibiting an IL of ~2.6 dB at the Xbar operating wavelength of 1563 nm. The residual ports of the fiber array were utilized to fan-out the 4 Xbar outputs that were converted to digital values via a multi-channel power meter (PM). The 50 um-long 50 GHz SiGe EAMs, that were deployed as intensity modulators for the encoding of both the input vector and the transformation matrix elements, introduced an IL of 4.5 dB also at the 1563 nm operating wavelength. Silicon-based TO PSs were utilized for the sign imprinting at every matrix node and for biasing Xbar’s nested MZIs. The Xbar chip, that occupies a total area of ~5.2 mm², was placed on a printed circuit board (PCB) that simplified the electrical interface between the electrically-controllable active components and the experimental testbed. More specifically, the DC pads of the SiPho chip were wirebonded in respective pads of the PCB and were routed to a break-out board through a ribbon cable.

A commercial laser source³⁶, a polarization controller and an 8-channel power meter³⁷ facilitated the experimental testing, while a custom-made multi-channel digital-to-analog converter (DAC) was utilized to fine tune the TO PSs and encode the targeted transformation matrix elements onto the Xbar nodes according to a look-up-table that correlates the matrix values to the EAM driving voltages.

Finally, it is worth noting that the optical path traversing the 4th column of the Xbar prototype introduced significant higher losses than expected, a result attributed to a damaged I/O coupler.

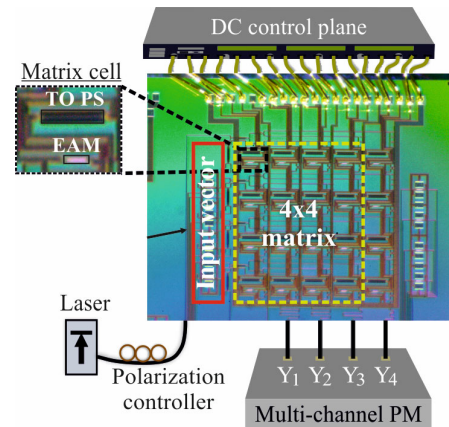


Fig. M1: Experimental setup for the characterization and programming of the 4×4 silicon photonic Crossbar. Inset: Elementary computing cell composed of a SiGe EAM and a Si TO PS.

Xbar programming using linear algebra

The HA programming model for each Xbar column was trained using #256 experimentally obtained linear transformations, corresponding to the 256 possible configurations when biasing the four constituent EAMs of each column in the range $B=[0,1,2,3]$. This led to an overdetermined system of linear algebraic equations whose independent variables were the summation of the IL of each Xbar row IL_r with the attenuation of each EAM $EAM_{ER_r}(V)$ when biased with a voltage $V \in B$. In order to solve this system, we enforced the least squares regression model³⁸. The least squares method is used to solve a linear system that has more equations than unknowns, by finding a solution that minimizes the sum of the squared errors between the expected and the experimentally obtained values, in contrast to simple linear algebra solvers that are designed to solve linear systems with a unique solution. More details on the complexity and the training requirements of the deployed model can be found in the Supplementary material.

Fidelity analysis of SoTA architecture

In order to quantify the fidelity degradation introduced by the differential optical path losses of the Clements architecture¹³, we calculated the achievable fidelity using a Monte-Carlo simulation analysis. Specifically, for different sets of circuit size N and node IL IL_{node} , with $N \in [4, 20]$ and $IL_{node} \in [0, 4.5]dB$, we generated 500 random unitary matrices U and following the decomposition method described in¹³, we concluded to its expected hardware implementation U_{exp} . Thereafter, we calculated the fidelity of the latter for each set of N and IL_{node} and fit the data into 2nd order polynomials to produce the curves shown in Fig. 4 (b).

Supplementary Material

This document provides supplementary material for the manuscript “**Perfect Linear Optics using Silicon Photonics**”.

A. Passive characterization of the 4×4 crossbar and its elementary device

The initial conditions of the employed calibration model referred to as the “baseline” model were derived through the experimental characterization of a standalone 50 um SiGe electro-absorption modulator (EAM). Figure S1 illustrates the experimentally measured insertion loss (IL) and the achieved static extinction ratio (ER) values when the EAM was reverse biased at a voltage level that ranged between 0 and 3V in steps of 0.5V, in the C-band transmission window. Followingly, the wavelength dependency of the 4x4 Xbar prototype was evaluated through tuning all the node phase shifters to perform fully-constructive interference and measuring the resulting optical spectrum response across all 4 Xbar column outputs. Figure S1(b) indicatively illustrates the acquired spectra for Column #2’s output, when all input vector EAMs were driven at 0V and all intra-column EAMs were biased at either 0V (blue curve) or 3V (orange curve). The observed resonant behavior can be avoided in future fabrication runs by matching the optical path lengths within the 4-branch multiport interferometer formed between the Xbar input and the column output. Fitting the acquired transfer functions envelope data to 2nd order polynomials, we calculate the IL and ER obtained for Xbar column#2 across the C-band. These metrics are plotted in Fig. 1(c) together with a figure-of-merit (FOM) that correlates ER and IL at the column output and is expressed as $FOM = ER(dB)/IL(dB)$. A maximum FOM of ~ 0.26 is obtained at $\lambda = 1563 \text{ nm}$, providing the optimum operational

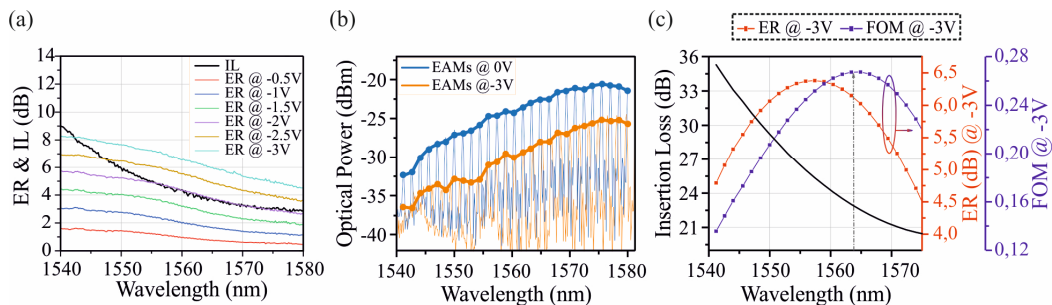


Fig. S1: (a) Standalone 50 um SiGe EAM characterization. Black solid line represents the insertion loss (dB), while colored solid lines correspond to the extinction ratio of the EAM at [-3, 0] V. (b) Optical spectrum of 4×4 Xbar’s column #2 when constituent EAMs are driven at 0 and -3V. (c) Fitted IL, ER and FOM of column 2.

wavelength.

B. Hardware aware programming model requirements

The first step of the 4×4 SiPho Xbar programming procedure, towards identifying the EAMs' performance deviation from the standalone EAMs measurements and every hardware mis-uniformity, included the experimental implementation of arbitrary linear transformations by biasing the #4 EAMs at each column with bias voltages in space $\mathbf{B} = \{0, -1, -2, -3\}V$. This experiment provided us with #256 ($=4^4$) different programming sets and #16 unknown parameters for each individual column, defined by the IL of each row (\mathbf{IL}_r) and the attenuation induced by the respective EAMs when biased with a voltage $V \in \mathbf{B}$. We express the unknown parameters in a 16-elements long vector of the form:

$\vec{\mathbf{B}} = [\mathbf{b}_1(0), \mathbf{b}_1(-1), \mathbf{b}_1(-2), \mathbf{b}_1(-3), \mathbf{b}_2(0), \dots, \mathbf{b}_4(-3)]$, with $\mathbf{b}_r(V)$, corresponding to the \mathbf{IL}_r + $\mathbf{EAM_ER}_r(V)$, of row $\#r \in \{1, 2, 3, 4\}$ when the respective EAM is biased at $V \in \mathbf{B}$ volts. The electric field linear summation of each practical set (i.e., each set comprises a unique combination of bias voltages applied to the EAMs of different rows) of $\vec{\mathbf{B}}$ with the all-one input vector would yield the

256-elements long vector $\vec{\mathbf{Y}} = \frac{1}{\sqrt{4}}[\mathbf{b}_1(0) + \mathbf{b}_2(0) + \mathbf{b}_3(0) + \mathbf{b}_4(0), \dots, \mathbf{b}_1(-3) + \mathbf{b}_2(-3) + \mathbf{b}_3(-3) + \mathbf{b}_4(-3)]$, which corresponds to the experimentally acquired values measured through our SiPho Xbar. Consequently, we create a 256:16 matrix T that is solely composed of zeros and ones as depicted in Fig. S2, with the non-zero elements dictating which bias voltage was applied in which row's EAM. For instance, the second row of the matrix T , indicates that the EAMs of the first three rows are bias at 0Vs, while the EAM of the last row is biased at -1Vs. Using $\vec{\mathbf{B}}$, $\vec{\mathbf{Y}}$ and T we can, then, approach the overparametrized system of linear equations (16 unknowns with 256 equations) as a linear algebra problem with $\vec{\mathbf{Y}} = \mathbf{T} * \vec{\mathbf{B}}$ and exploit a well-known linear regression method, such as the least square method, to approximate the solutions $\vec{\mathbf{B}} = ((\mathbf{T}^T * \mathbf{T})^{-1} * \mathbf{T}^T) * \vec{\mathbf{Y}}$ and establish the

	$\mathbf{IL}_1 + \mathbf{EAM_ER}_1$				$\mathbf{IL}_2 + \mathbf{EAM_ER}_2$				$\mathbf{IL}_3 + \mathbf{EAM_ER}_3$				$\mathbf{IL}_4 + \mathbf{EAM_ER}_4$			
$\vec{\mathbf{B}}$:	$\mathbf{b}_1(0)$	$\mathbf{b}_1(-1)$	$\mathbf{b}_1(-2)$	$\mathbf{b}_1(-3)$	$\mathbf{b}_2(0)$	$\mathbf{b}_2(-1)$	$\mathbf{b}_2(-2)$	$\mathbf{b}_2(-3)$	$\mathbf{b}_3(0)$	$\mathbf{b}_3(-1)$	$\mathbf{b}_3(-2)$	$\mathbf{b}_3(-3)$	$\mathbf{b}_4(0)$	$\mathbf{b}_4(-1)$	$\mathbf{b}_4(-2)$	$\mathbf{b}_4(-3)$
Sets	1	0	0	0	1	0	0	0	1	0	0	0	1	0	0	0
	1	0	0	0	1	0	0	0	1	0	0	0	0	1	0	0
	1	0	0	0	1	0	0	0	1	0	0	0	0	0	1	0
[T]:	0	0	0	1	0	0	0	1	0	0	0	1	0	0	0	1

Fig. S2: Visual representation of the system of linear algebra matrices created to approximate the behavior of Xbar specifications (passive and active components).

final look-up tables.

Towards quantifying the programming complexity and the convergence credentials of the employed HA calibration method, we performed a simulation analysis where we trained the HA model using only part of the calibrating dataset, yet always keeping the length of the utilized dataset greater than the number of the unknown parameters (>16). The absolute programming error of the model was then recorded. More specifically, we split the calibration dataset in two parts with the 80% being utilized for calibrating the model and the residual 20% for validation. The dataset employed for calibration purposes was formed by firstly selecting 16 linear transformations, where all the unknown parameters are contributing and, subsequently, adding random samples of the remaining batch. At each step, we record the absolute programming error of each Xbar column. The simulation results are depicted in

Fig. S3. The errors calculated at columns 1-4 are illustrated with the blue, orange, red and green bold solid curves, respectively, while their minimum error is highlighted by the respective horizontal light solid lines. As observed, in the best case the minimum absolute programming error can be achieved using less than 5%, on top of the required #16, samples from the training dataset, with the worst case

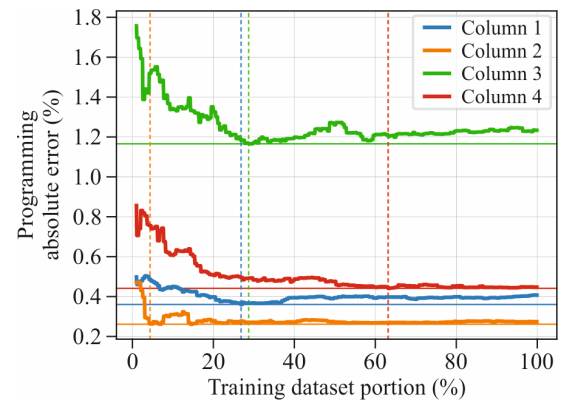


Fig. S3: Quantitative illustration of calibration model's dataset length requirement towards achieving the minimum absolute programming error at each Xbar column. X-axis: Percentage of the #240 linear transformations dataset capitalized to train Xbar's calibration model.

requiring $\sim 63\%$ extra samples. This can be translated to a minimum required dataset comprising 10-65% of the 256 experimentally obtained samples. Setting an error margin of 10% relative to the minimum achieved error, reveals that even when using $<17\%$ of the acquired 256 measurements, high converge and low absolute error can still be achieved.

C. Power consumption analysis

The deployment of SiGe EAMs for the encoding of the input vector and transformation matrix elements, apart from the high bandwidth of >50 GHz, equips the Xbar architecture with ultra-high energy efficient computing nodes. The static power consumption of the EAMs can be calculated

through $EAM_{static} = \left(\frac{1}{2}\right) * P_{in,mW} * R * V_{static} = 24 \mu W$ [1], with $P_{in,mW}$ corresponding to the incident power at the EAM input port equal to ~ 3 mW, R the responsivity of the device of $R = 0.8 A/W$, and V_{static} the average driving voltage, equal to 1.5 V when considering a uniform distribution in the range B[0-3]. This translates into a Xbar transformation matrix power consumption of only < 0.4 mW.

Operating the EAM nodes dynamically, would unlock several capabilities [2] and applications where the Xbar architecture can be employed. Assuming a driving voltage of 1 Vpp, each EAM operating at 50 GHz would consume $EAM_{dynamic} = CR * \left(\frac{1}{4}\right) * C * V_{dynamic}^2 = 0.25 mW$ on top of its static power consumption, concluding to an overall average Xbar transformation matrix power consumption of ~ 4.4 mW. It is worth mentioning that in the case of unbalanced arms between the nested MZIs' arms, the power consumption of the Xbar transformation matrix programming should, also, include the energy consumed to tune the silicon TO PSs, requiring 4 mWs for a full π -shift each.

References

1. M. Pantouvaki, et. al., "Active Components for 50 Gb/s NRZ-OOK Optical Interconnects in a Silicon Photonics Platform." Journal of Lightwave Technology, vol. 35, no. 4, pp. 631-638 (2017).
2. G. Giamougiannis et al., "Universal Linear Optics Revisited: New Perspectives for Neuromorphic Computing With Silicon Photonics," in IEEE Journal of Selected Topics in Quantum Electronics, vol. 29, no. 2: Optical Computing, pp. 1-16, March-April 2023, Art no. 6200116, doi: 10.1109/JSTQE.2022.3228318.